scientific reports

OPEN

Enhancing the stability and efficiency of dye-sensitized solar cells with MIL-125 metal-organic framework as an electrolyte additive

Ayagoz Ibrayeva[1,2], Zulfiya Imanbekova[3], Urker Abibulla[3], Yerbolat Tashenov[2], Bakhytzhan Baptayev[1]✉ & Mannix P. Balanay[1,3]✉

This study investigates how to improve the stability of liquid electrolyte (LE) dye-sensitized solar cells (DSSCs) by incorporating a titanium-based metal-organic framework (MIL-125). MIL-125, created through the coordination of Ti^{4+} ions with benzene-1,4-dicarboxylic acid, forms a structure that can effectively accommodate I^-/I_3^- electrolytes, resulting in a MIL-125@electrolyte assembly. This innovative assembly successfully prevents electrolyte leakage while preserving the LE properties. The study examines how the MIL-125@electrolyte enhances both stability and power conversion efficiency (PCE) of DSSCs. The inclusion of the large-surface-area of MIL-125 improves ionic conductivity, reduces charge transfer resistance, and stops leakage. The optimized MIL-125@electrolyte achieves a high PCE of 10.51%, with a peak value of 10.99%, and a notable short-circuit current density of 20.97 mA/cm², peaking at 22.27 mA/cm², under standard AM 1.5, 100 mW/cm² conditions. It maintains about 75% of its PCE after 1400 h at approximately 23 °C. For indoor applications using LED lighting, the quasi-solid-state DSSC reaches a record PCE of 27.6%, with an average of 25.9%, under 6000 lx illumination.

Keywords Metal-organic frameworks, MIL-125, Quasi-solid-state electrolytes, Dye-sensitized solar cells, Indoor photovoltaics

Liquid electrolytes (LE) are still very efficient for DSSCs, as recent advances show. The highest PCE of 15.2% under a standard air mass of 1.5 global simulated sunlight was achieved with LE[1], and a record PCE of 34% at dimmed indoor fluorescent light (1000 lx) was also obtained with LE[2]. However, despite its excellent performance, LE presents challenges such as corrosion, volatility, and leakage, which hinder the commercialization of DSSCs due to long-term operational limitations[3]. Efforts are underway to replace the LE with quasi-solid and solid-state electrolytes to address these stability issues. Solid-state hole transport materials (HTMs) could solve the problems of leakage and sealing, but face problems such as poor pore filling, electron recombination at the photoanode interface, and low conductivity, requiring thorough engineering solutions. Quasi-solid-state electrolytes (QSE) are promising as they combine the advantages of LE with the long-term stability of DSSCs. The redox couple commonly used in LE, the iodide/triiodide couple (I^-/I_3^-), is also used in QSE[4], in which the redox couple is enclosed or incorporated in a closed polymer chain or frame with a large surface area. Several recent studies have investigated different materials for QSE, including ionic polymer liquid (PCE:9.83%)[5], Al_2O_3(PCE:8.74%) and ZnO nanofillers (PCE:7.59%)[6], Ti_3C_2MXene-reduced graphene oxide composite (PCE:8.26%)[7], PEG-functionalized ABA triblock copolymers (PCE:10.02%)[8], SiO_2aerogel with graphene as a framework (PCE:8.25%)[9].

Metal-organic frameworks (MOFs) offer exceptional chemical diversity due to their unique structure and adjustable organic and inorganic components. This versatility allows for applications across various fields, including magnetism, ferroelectricity, light harvesting, energy transfer, optoelectronics, sensors, and gas management, as well as (photo)catalysis and drug delivery[10]. Recently, the use of MOFs in DSSCs has garnered

[1]National Laboratory Astana, Nazarbayev University, 53 Kabanbay Batyr Ave, Astana 010000, Kazakhstan. [2]Department of Chemistry, L.N. Gumilyov Eurasian National University, 2 Satpayev St, Astana 010008, Kazakhstan. [3]Chemistry Department, Nazarbayev University, 53 Kabanbay Batyr Ave, Astana 010000, Kazakhstan. ✉email: ; mannix.balanay@nu.edu.kz

increasing attention[11]. Researchers are exploring MOFs to enhance the components of DSSCs, including photosensitizers[12–14], photoanodes[15–21], and counter electrodes[22–24], to boost efficiency. Studies indicate that MOFs can serve as charge transfer materials, improving dye adsorption and light scattering due to their high porosity and surface area, which in turn enhances photovoltaic performance. Furthermore, MOFs may enhance electron transport and reduce dark current when combined with materials like reduced graphene oxide[15].

MOFs have proven to be another promising scaffold material for QSE, as they provide a large surface area for LE uptake. The first use of MOF-based QSEs was reported by Bella and colleagues[25], who used a polymer composite containing Mg-MOF as a scaffold for QSEs for DSSCs, which exhibited a PCE of 4.80%. The presence of Mg-MOF improved the stability of the DSSCs, with 96% of PCE retained after 500 h. In a similar study, Sarwar et al.[26] demonstrated a successful application of a MOF prepared from the reaction of Al^{3+} and trimesic acid. The Al-MOF-based gel electrolyte was reported to retain the function of a LE and exhibit higher cell efficiency and remarkable device stability at a thermal load of 60 °C for 250 h compared to LE based DSSCs with a maximum PCE of 6.06%. However, the introduction of a metal cation at the interface between the photoanode and electrolyte may affect the conduction band of the TiO_2 semiconductor, potentially reducing the $V_{OC}$of the DSSCs[28,29].

This study highlights the promising potential of further research into MOFs for photovoltaic applications, particularly as customizable materials to improve device components. The approach focuses on the use of Ti-based MIL-125 as a scaffold for I^-/I_3^-based LE to prevent leakage and improve the lifetime and stability of electrons in DSSCs. While MOFs have been extensively researched in DSSCs, their effects on LE remain unclear, emphasizing the critical role of the metal component in MOFs at this interface. This research does not suggest new applications but emphasizes the significant potential of MOFs as charge carriers due to their special chemical and photophysical properties. The study presents innovative methods using MIL-125 as a scaffold to create a QSE that minimizes electrolyte leakage, increases electron lifetime, and preserves the conduction band of TiO_2 while preventing dye degradation. To understand the importance of MOFs with suitable pore sizes and large surface areas for the formation of QSEs, a comprehensive analysis of DSSCs devices is required. This investigation aims to fill gaps in the literature by thoroughly investigating the synthesis, properties, and effects of MIL-125 on DSSCs performance under both outdoor and indoor conditions.

Materials and methods

Materials

All the chemicals used in this study were of high purity from commercial sources and used without further purification unless otherwise specified. Fluorine-doped SnO_2 (FTO) coated glass (7 Ω/sq, 2.2 mm, Sigma Aldrich); light scattering titania paste (Greatcell Solar WER2-O TiO_2 Paste, Sigma-Aldrich); transparent TiO_2 electrode paste (DN-EP03, Dyenamo); screen printable Platinum paste (Greatcell Solar PT1 Pt paste, Sigma-Aldrich); Di-tetrabutylammonium cis-bis(isothiocyanato)bis(2,2’-bipyridyl-4,4’-dicarboxylato)ruthenium (II), 95% (N719, Sigma Aldrich); chenodeoxycholic acid (CDCA, Sigma Aldrich); terephthalic acid, 98% (Sigma Aldrich); titanium (IV) isopropoxide, 97% (TTIP) Sigma Aldrich); N,N’-dimethylformamide, anhydrous, 99.8% (DMF, Sigma Aldrich); methanol, ≥ 99.9% (MeOH, Honeywell); iodine ≥ 99,8% (Sigma Aldrich); lithium iodide, 99.9% (LiI, Sigma Aldrich); guanidine thiocyanate, 99% (GuSCN, Alfa Aesar, Thermo Scientific); 1-butyl-3-methylimidazolium iodide (BMII, DN-OD05, Dyenamo); 3-methoxypropionitrile (MPN, Sigma Aldrich); 4-tert-butylpyridine, 98% (tBP, Sigma Aldrich); acetonitrile (ACN, Acros Organic); tert-butanol, ≥ 99.0% (Sigma Aldrich); and hydrochloric acid > 37% (HDL, Sigma Aldrich).

Preparation of MIL-125-based quasi-solid-state electrolyte

Synthesis of MIL-125

A solvothermal technique based on the literature was used to synthesize MIL-125 [15]. 1.26 g of terephthalic acid was dissolved in 20 mL DMF and 5 mL MeOH for this purpose. After 15 min of stirring, the mixture was heated to 100 °C. Next, the mixture was mixed with 1.5 mL of titanium isopropoxide and 0.09 mL of water. To produce a white product, the reaction mixture was heated to 100 °C for 35 h. Centrifugation (8,000 rpm, 15 min) was used to extract the product from the mixture, and it was then washed six times in MeOH and three times in DMF.

Electrolyte preparation. The composition of a typical LE is as follows: 0.03 M I_2, 0.05 M LiI, 0.10 M GuSCN, 0.6 M BMII, 0.5 M tBP in ACN: MPN (1:1). To prepare the QSE various concentrations of MIL-125 ranging from 20 mg/mL to 60 mg/mL were tested, with careful monitoring to ensure uniformity of the electrolyte. To prevent aggregation and achieve uniform particle dispersion, MIL-125 was first dispersed in the solvent using ultrasonication for 30 min for each trial. The optimal combination for the QSE was found to be 10 mg of MIL-125 activated at 150 °C, mixed with 0.5 mL of LE, and stirred at room temperature in a closed vessel (Table S1, supporting information). The electrolytes were stored in sealed containers in the dark with continuous stirring. It was observed that higher concentrations led to decreased efficiency in DSSCs due to increased viscosity and particle aggregation, which in turn reduced ion mobility. Images of the prepared QSE are shown in Figure S1 (supporting information).

Fabrication of dye-sensitized solar cells

After immersing in a 50 mM aqueous TTIP solution in 2 M aqueous HCl at 70 °C for 35 min, the 1.5 × 2.0 cm conductive FTO glass electrodes underwent rinsing with DI water and sintering at 500 °C for 30 min. Subsequently, a transparent TiO_2 paste (particle size: 18–20 nm) was applied using a doctor blade technique onto the prepared film. The TiO_2 film underwent a gradual sintering process: initially at 125 °C for 5 min, followed by 325 °C for 10 min, 425 °C for 15 min, and finally 500 °C for 30 min, after an initial hour of air drying. A scattering TiO_2 film (particle size: 150–250 nm) was then doctor-bladed onto the transparent TiO_2 film. After another hour of air drying, this second layer was sintered using the same step-by-step procedure as the transparent TiO_2 layer.

Following sintering, the photoanodes were cooled to 70 °C and soaked for 24 h at room temperature in the dark with 0.25 mM of N719 dye in tert-butanol: acetonitrile (1:1) solution containing 0.75 mM chenodeoxycholic acid. The dye-coated photoanodes were subsequently dried in an oven at 70 °C after rinsing with ethanol. Simultaneously, a clean FTO glass was coated with Pt paste and heated to 500 °C for 30 min to create the counter electrodes (CE). The assembly of the photoanode and CE took place in a sandwich configuration using double-sided tape as a spacer, facilitating the placement of either liquid or quasi-solid electrolytes between them via a drop-casting technique.

Characterization

MIL-125 underwent characterization using various analytical techniques. X-ray diffraction (XRD) analysis was conducted using a Rigaku SmartLab device in Cedar Park, Texas, USA. Fourier-transform infrared (FT-IR) spectroscopy was performed using a ThermoScientific NicoletTM iS5 spectrometer. Thermal analysis was carried out using a TA Instruments TGA Q500 thermogravimetric analyzer (TGA). Morphological and compositional investigations were conducted using a JEOL JEM-1400 Plus transmission electron microscope (TEM) and a Carl Zeiss SEM Auriga Crossbeam 540 scanning electron microscope (SEM) equipped with an energy-dispersive X-ray spectrometer. Thermo Scientific's NEXSA X-ray photoelectron spectrometer (XPS) was employed to analyze the valence states of elements. Nitrogen adsorption-desorption analysis was performed using a porosimeter from Quantachrome Instruments. The photovoltaic performance of DSSCs was evaluated using an AAA solar simulator (Oriel Sol3A by Newport), with electrochemical studies conducted using a Palmsens4 potentiostat. Device I-V characteristics were measured using a Keithley 2440 source meter under an Oriel Sol3A class solar simulator with an AM 1.5G filter of 100 mW/cm² with a 0.03 cm² mask during photovoltaic performance testing of DSSCs. Light intensity was measured using a calibrated Oriel Si reference cell system (Model: 91150 V Reference Cell and Meter). Each sample underwent the preparation of five cells and reported photovoltaic parameters represent average values. Electrochemical impedance spectroscopy (EIS) was conducted on DSSCs in total darkness, with similar tests on dummy cells under different conditions.

Results and discussion

Characterization of MIL-125

The X-ray diffraction pattern depicted in Fig. 1a for the synthesized metal-organic framework exhibits distinct diffraction peaks at 6.81°, 9.75°, 11.67°, 13.67°, 15.03°, 15.42°, 16.62°, 17.93°, 19.02°, and 19.55° which were attributed to (101), (200), (221), (220), (310), (103), (222), (312), (213), and (400) lattice planes closely resembling the diffraction pattern of MIL-125 [30,31]. The absence of additional peaks in the XRD pattern confirms the high purity of the synthesized MOF product. MIL-125 is known for its quasi-cubic tetragonal system, composed of octameric $Ti_8O_8(OH)_4$ oxo-clusters interconnected with dicarboxylate linkers.

Further analysis through Fourier-transform infrared spectroscopy, as shown in Fig. 1b, reveals the characteristic features of the MIL-125 at the fingerprint region are observed in the range of 800–1200 cm^{-1} for absorption of benzene rings, while at the 400–800 cm^{-1}range is a characteristic feature of the O-Ti-O vibrations[32]. The peak at 3395 cm^{-1}belongs to the O-H stretching vibration[33]. Signals within the range of 1584–1392 cm^{-1} are ascribed to aryl vibrations and carboxylate functional groups[34].

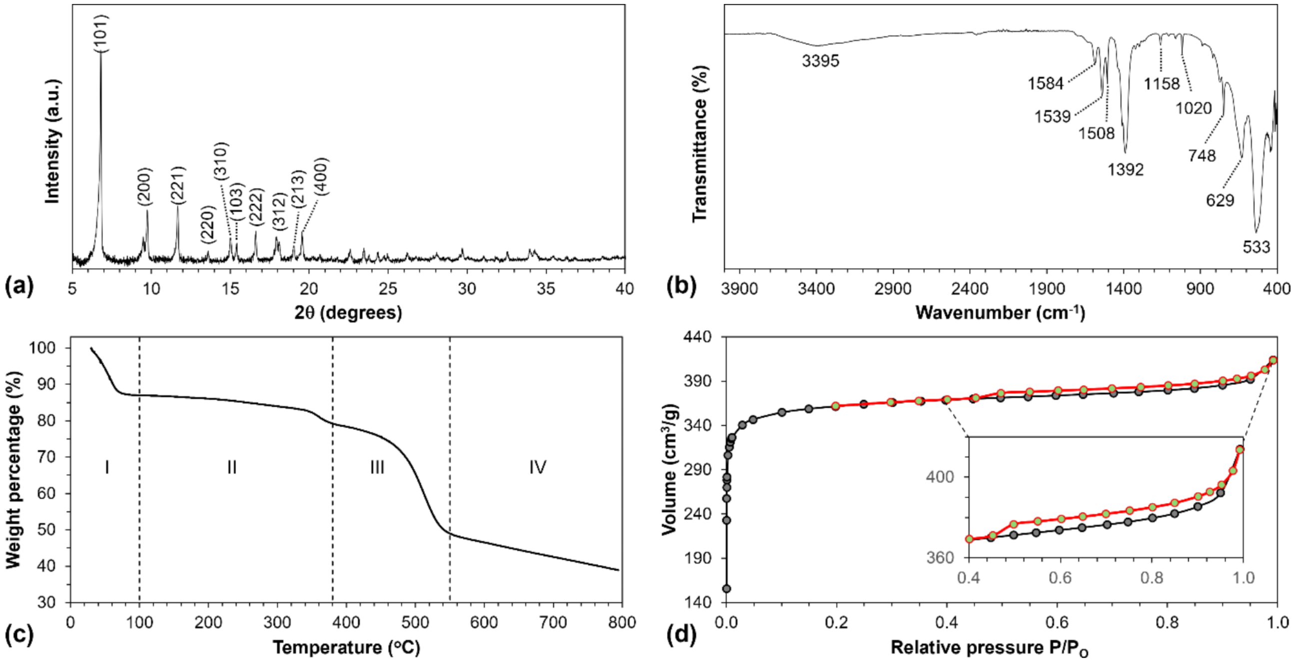

Fig. 1. (**a**) Powder XRD profile, (**b**) FT-IR Spectra, (**c**) TGA curve, and (**d**) N_2 sorption isotherm of MIL-125.

The thermogravimetric analysis shown in Fig. 1c highlights four distinct stages of weight loss. In the first stage, which occurs below 100 °C, there is a 13% reduction in weight. This loss is attributed to the removal of guest molecules, including moisture, methanol, and some residual DMF trapped in the pores of MIL-125. The second stage, marked by an 8% weight loss, is associated with the further removal of residual DMF[35]. The most substantial weight loss, between 380 °C and 550 °C, amounts to 30% and is primarily due to the decomposition of organic linkers, resulting in the formation of inorganic titanium oxide residues[36].

The ratio of titanium to TiO_2can be calculated by dividing the weight loss at 550 °C by the weight loss at 380 °C, which represents the onset of organic linker decomposition[37]. This ratio was found to be approximately 62%. Finally, the weight loss observed above 550 °C is likely due to the removal of hydroxyl groups on the surface of the TiO_2[38]. The nitrogen porosimetry data (Fig. 1d) reveals a Type I isotherm with minimal hysteresis, indicating a well-ordered microporous structure[39]. This structure has a micropore volume (V_p) of 0.61 cm^3 g^{-1} and a high Brunauer–Emmett–Teller (BET) surface area of 1452 m^2 g^{-1}. Characterization using scanning electron microscopy and transmission electron microscopy (Fig. 2a and b) shows the development of a cake-like morphology with diameters ranging from 750 to 900 nm. Additionally, energy-dispersive X-ray spectroscopy mapping confirms the uniform distribution and coexistence of titanium, oxygen, and carbon in MIL-125 (Fig. 2c).

To investigate the local electronic structure and oxidation state of the synthesized MIL-125, LE conducted X-ray photoelectron spectroscopy, as depicted in Fig. 3. The analysis revealed three prominent peaks corresponding to C 1s, Ti 2p, and O 1s, further confirming the successful synthesis of MIL-125 (Fig. 3a). The high-resolution XPS spectra for C 1s, shown in Fig. 3b, display three distinct peaks at 283.6, 285.0, and 287.5 eV,

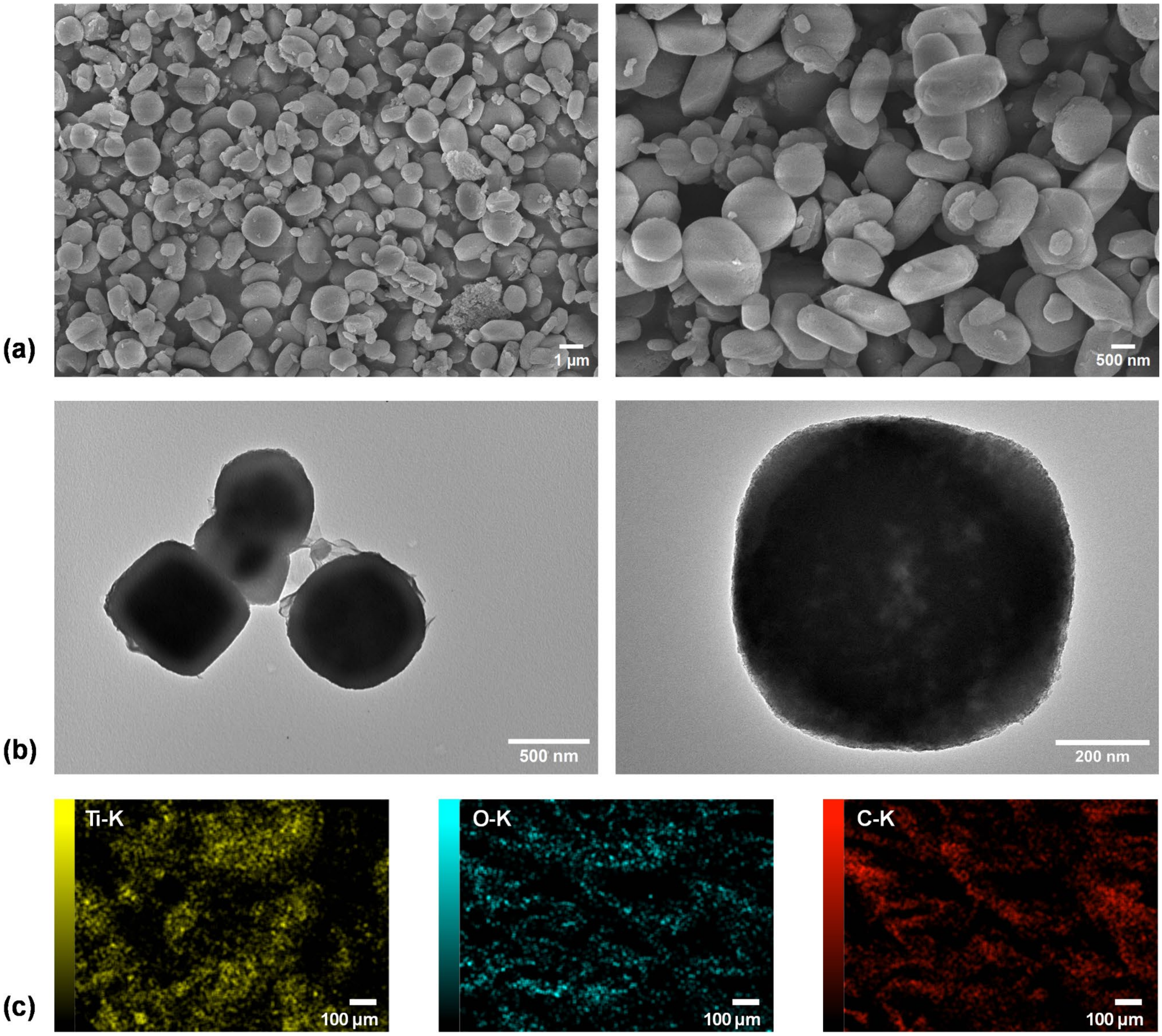

Fig. 2. (**a**) SEM and (**b**) TEM images of MIL-125 at various magnifications. (**c**) Elemental mapping of MIL-125.

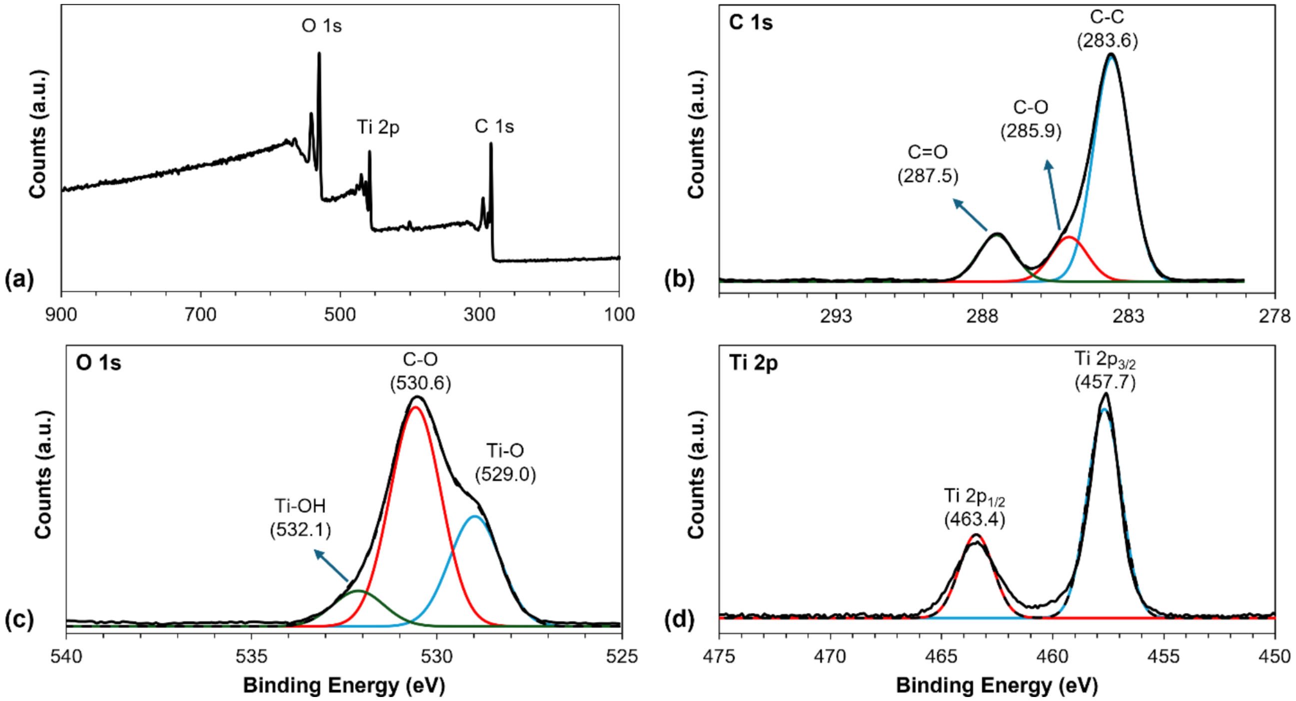

Fig. 3. (**a**) XPS survey scan and high resolution XPS spectra of (**b**) C 1s, (**c**) O 1s, and (**d**) Ti 2p for MIL-125.

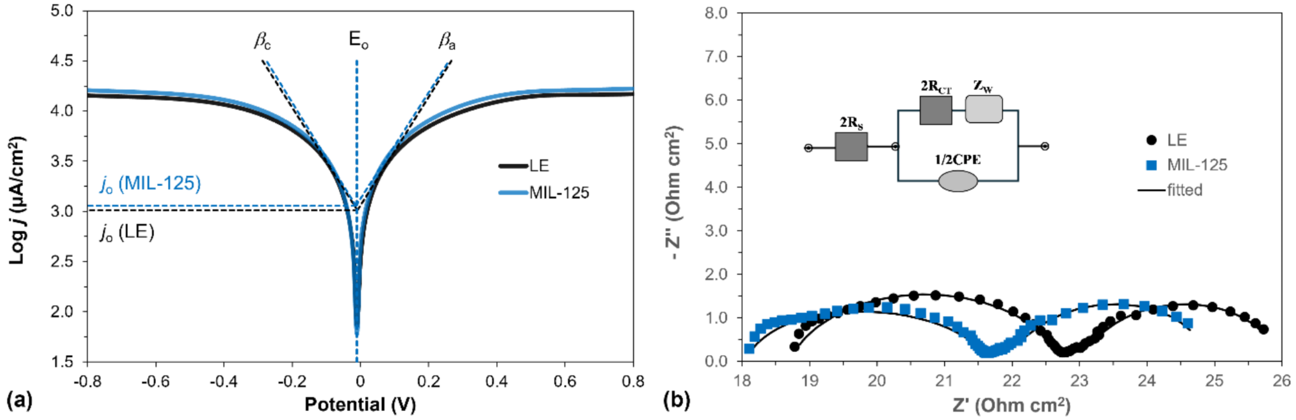

Fig. 4. (**a**) Tafel polarization curves of LE and MIL-125 (**b**) Nyquist plot of symmetrical dummy cells (inset is the equivalent electrical circuit used for fitting of Nyquist plots).

which are attributed to C-C, C-O, and C = O bonds, respectively[40]. Figure 3c presents the O 1s spectra, which can be deconvoluted into three peaks at 529.0, 530.6, and 532.1 eV, corresponding to Ti-O, C-O, and Ti-OH bonds, respectively[41]. Additionally, the Ti $2p_{3/2}$ and Ti $2p_{1/2}$ peaks are observed at 457.7 and 463.4 eV, respectively (Fig. 3d), indicating the successful incorporation of Ti^{4+} ions into the MIL-125 structure.

Electrochemical analysis of MIL-125-based quasi-solid electrolyte

The charge-transfer kinetics at the interface between the QSE and the platinized CE were investigated using Tafel analysis (Fig. 4a). The rates of the redox reactions occurring at this interface can be characterized by the Butler–Volmer equation as presented in Eqs. 1[42–44].

$$j = -j_o \left[\exp \frac{\alpha_c nF}{RT} (E - E_{eq}) - \exp \frac{-\alpha_a nF}{RT} (E - E_{eq}) \right] \tag{1}$$

where j is the electrode current density, j_o is the exchange current density, E is the applied voltage, E_{eq} is the I^-/I_3^- electrode potential at equilibrium, n is the number of electrons transferred, F is Faraday constant, α_c, and α_a are the cathodic and anodic charge-transfer coefficients, respectively, R is the universal gas constant,

T is the absolute temperature. (E–E_{eq}) is defined as activation overpotential. When $|E–E_{eq}| \gg 0$, Eq. 1 can be transformed into the original Tafel equation as shown in Eq. 2[45].

$$E - E_{eq} = \pm\,\beta\,\log_{10}\frac{j}{j_o} \tag{2}$$

where is the Tafel slope, the slope of the linear regions of the Tafel polarization curve, and indicates how much the overpotential must be increased to enhance the reaction rate (or current) of an electrochemical reaction by a factor of ten. The anodic slope (β_a) and cathodic slope (β_c) provide insights into the anodic and cathodic reactions taking place at the TiO_2/electrolyte interface. The Tafel polarization tests on $3I^-/I_3^-$redox reaction were done in the potential range between ± 1 at a scan rate of 50 mV/s. For this analysis, a symmetric cell with two identical Pt electrodes with an active area of 0.25 cm[2] was assembled with different electrolytes used in the DSSCs. The anodic and cathodic slope values reflect the anodic and cathodic reactions occurring at the TiO_2/electrolyte interface. In the case of the QSE, the cathodic Tafel slope was lower ($\beta_c = 181$ mV/decade) compared to the LE ($\beta_c = 186$ mV/decade). This suggests that the gelation of the electrolyte in QSE enhances the reaction of I_3^- ions at the TiO_2/electrolyte interface. Conversely, the anodic Tafel slope was slightly higher in QSE ($\beta_a = 188$ mV/decade) than in LE ($\beta_a = 185$ mV/decade), which could indicate a minor decrease in the reaction of I^- ions at the interface. The gelation of the electrolyte increases its viscosity, which in turn affects the movement of ions through it. Our results show that I_3^- becomes more prominent because its reactions with the TiO_2 surface typically occur at a higher rate compared to I^- ions.

From Eq. 2, it follows that $j = j_o$ when the overpotential is at its equilibrium value. The j_o value is determined by the intercept of the linear anodic and cathodic branches on the Tafel plot. For the LE, j_o is 1.02 mA/cm², while for the QSE, it is 1.14 mA/cm². This indicates that the electron flow at the TiO_2/QSE interface is higher compared to the TiO_2/LE interface. Additionally, j_o is related to the charge transfer resistance R_{CT} at the interface, as described by Eq. 3.

$$j_o = \frac{RT}{nFR_{CT}} \tag{3}$$

The charge-transfer resistance can be determined through electrochemical analysis of a symmetrical dummy cell, where two identical electrodes (Pt CE) are positioned face-to-face, with an electrolyte sample filling the gap between them. Figure 4b illustrates the Nyquist plot for these symmetrical dummy cells using QSE and LE. In the Nyquist plot, the x-axis intercept represents the series resistance (R_S), the first semicircle denotes the charge-transfer resistance (R_{CT}), the second semicircle indicates the diffusion resistance of the electrolyte (Z_W), and CPE is a constant phase element that accounts for deviations from ideal capacitance caused by the roughness of the electrode surfaces[46]. The charge-transfer resistance for QSE is significantly lower than that for LE, measuring 1.79 Ohms compared to 1.99 Ohms, which is consistent with the results obtained by the Tafel experiments. Using these values, the ionic conductivity (σ) of the electrolyte films can be calculated according to Eq. 4,

$$\sigma \;=\; \frac{d}{R_{CT}A} \;= nq\mu \tag{4}$$

where d and A are the thickness and area of the electrolyte layer, n is the charge carrier concentration, q represents the charge on the mobile carrier, and $\mu$is the carrier mobility[47]. From our results, it was found that the QSE demonstrates higher conductivity (3.36 mS/cm) compared to the LE (3.02 mS/cm). According to Eq. 4, the increased conductivity could be attributed to either a higher carrier mobility, an increase in charge carrier concentration, or a combination of both factors which was observed in previous studies[26,28,48].

Photovoltaic performance of MIL-125-based quasi-solid electrolyte

A DSSCs was fabricated using an electrolyte enriched with MIL-125, and its electrochemical and photovoltaic parameters were evaluated as shown in Table 1. For comparison, a DSSCs with a conventional LE was also fabricated as a control device. The DSSCs with QSE showed a remarkable improvement in energy conversion efficiency, reaching 10.51% compared to 9.14% for the cell with the LE. This improvement is primarily due to the higher short-circuit current density in the QSE, which was 20.97 mA/cm², compared to 18.01 mA/cm² for the LE cell. This difference was confirmed by incident photon power efficiency (IPCE) measurements (Fig. 5a), which showed that the short-circuit current density derived from the IPCE curve for the QSE was 20.9 mA/cm², exceeding the 17.1 mA/cm² observed for the LE DSSCs.

Electrochemical impedance spectroscopy was conducted under dark conditions with a bias voltage close to the Voc, spanning a frequency range from 0.01 Hz to 1 MHz, to assess the interfacial properties of the fabricated QSE in DSSCs, as illustrated in Fig. 5b. In the dark, under the applied bias voltage, electrons flow from the photoanode to the electrolyte and recombine with I_3^-, resulting in I^- being oxidized at the CE. In the Nyquist plot, the impedance related to recombination is represented by a large semicircle in the moderate

Electrolytes	J_{SC} (mA/cm^2)	V_{OC} (V)	FF (%)	PCE (%)	J_{SC} from IPCE (mA/cm^2)	R_S (Ω)	R'_{CT} (Ω)	R_{rec} (Ω)	τ_{rec} (msec)
LE	18.01	0.71	0.72	9.14	17.1	23.7	12.9	122.5	108
QSE	20.97	0.69	0.72	10.51	20.9	28.9	8.8	57.3	57

Table 1. Photovoltaic parameters of devices under 1 sun (100 mW/cm^2) condition.

Metal(organic linker) of MOF	Redox couple	Dye (soaking time in hours)	Active surface area (cm^2)	PCE (%)	Ref.
Co(BDC)[b]	$[Cu(bnbip)(mpi)^{+1/+2}]$[c, d]	0.5 mM N719 with 0.5 mM CDCA in EtOH (24)	0.36	3.45	[51]
Al(BTC)[e]	I^-/I_3^-	N719 (16) [f]	0.16	8.69	[28]
Al(BTC)[e]	I^-/I_3^-	0.3 mM N719 in EtOH (21)	0.25	6.06	[26]
Mg(BTC)[e]	I^-/I_3^-	0.35 mM N719 in EtOH (12)	0.22	4.80	[25]
Mn(BTC)[e]	I^-/I_3^-	N719 in MeCN: isopropanol [f]	–	5.45	[52]
Ti(BDC)[b]	I^-/I_3^-	0.25 mM N719 and 0.75 mM CDCA in t-BuOH: MeCN (24)	0.03	10.51	This work

Table 2. Comparison of literature of DSSCs incorporating MOFs as additives in the electrolyte [a].

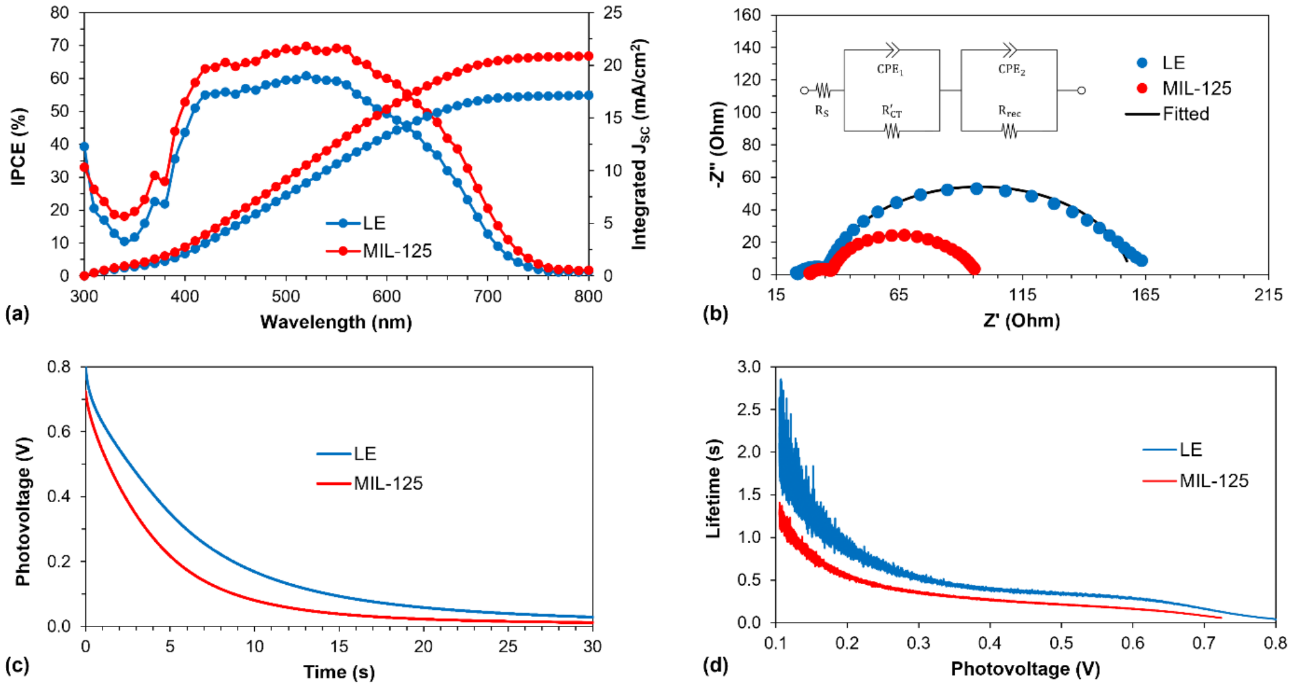

Fig. 5. (**a**) IPCE spectra and integrated J_{SC} curve, (**b**) Nyquist plot (inset is the equivalent electrical circuit used for fitting of Nyquist plots), (**c**) open-circuit voltage decay curves, and (**d**) electron lifetime vs. photovoltage dependence of DSSCs with QSE- and LE-based electrolytes.

and low-frequency regions. Conversely, a small semicircle at high frequencies represents the charge transfer impedance at the LE/CE interface. Analysis of these semicircles yields the charge transfer resistance (R'_{CT}) and recombination resistance (R_{rec}) as detailed in Table 1. The inclusion of MIL-125 in the LE led to a decrease in the charge transfer resistance at the CE/QSE interface compared to the CE/LE, indicating enhanced electron flow from the platinized fluorine-doped tin oxide electrode into the QSE. This finding aligns with the results from Tafel polarization and Nyquist plot analysis of symmetrical dummy cells. Notably, the MIL-125-based QSE DSSCs exhibited a significant reduction in recombination resistance, from 122.5 Ω for LE to 57.3 Ω for QSE. The recombination resistance and chemical capacitance allow for the calculation of the recombination lifetime (τ_{rec}) for both types of DSSCs, as described by Eq. 5[49].

$$\tau_{rec} = R_{rec} \times C_{\mu} \tag{5}$$

As a result, the recombination lifetime for QSE decreased by nearly 50% compared to that of LE cells. To further investigate this phenomenon, a Voc decay analysis was performed (Fig. 5c). The decay curve obtained from this analysis was then used to calculate the electron lifetime at various Voc using Eq. 6.

$$\tau_{e} = \left(\frac{k_b T}{q}\right)\left(\frac{dV}{dt}\right)^{-1} \tag{6}$$

where k_b is Boltzmann constant, T is absolute temperature, q is elementary charge, V is voltage, and t is time. The calculated lifetime reflects the effective duration of conduction band electrons. Figure 5d shows that the electron lifetime in QSE-based DSSCs is shorter than that in LE-based devices, indicating a higher rate of electron

Electrolytes	Illuminance (lux)	J_{SC} (mA/cm^2)	V_{OC} (V)	FF	PCE (%)
	1032 ± 19	47.03	0.64	0.66	7.87 (11.08)
LE	3047 ± 13	155.76	0.69	0.71	14.47 (18.58)
	6024 ± 39	341.52	0.73	0.73	16.94 (21.29)
	1032 ± 19	86.11	0.55	0.59	11.10 (12.12)
QSE	3047 ± 13	255.37	0.62	0.68	20.24 (21.03)
	6024 ± 39	582.9	0.65	0.73	25.90 (27.60)

Table 3. Photovoltaic metrics of the DSSCs for indoor – light conditions.

CDCA content (mM)	Electrolyte Solvent	Electrolyte additives	Light source	PCE (%)	Ref.
0	CAN	BMII, GuNCS, and TBP	T5 fluorescent lamp	21.6	[53]
1	ACN/MPN (80 : 20 v/v)	DMPI, TBP	T5 fluorescent lamp	27.64	[54]
0	ACN/MPN (8/2)	DMPII, tBP and POEI-TEMPO (0–30 wt%)	T5 fluorescent lamp	25.99	[5]
0	ACN/VN, 85/15	PMII, TBP	LED	17.63	[55]
0	ACN/VN, 85/15	PMII, TBP	T5 fluorescent lamp	18.91	[55]
0	ACN/VN, 85/15	PMII, TBP, TBAI	T5 fluorescent lamp	15.12	[56]
0	ACN/VN, 85/15	PMII, TBP	T5 fluorescent lamp	24.00	[57]
0	ACN/VN, 85/15	PMII, TBP	T5 fluorescent lamp	26.85	[58]
0.75	ACN/MPN, 50/50	BMII, TBP, GuSCN	LED	21.29	This work
0.75	ACN/MPN, 50/50	BMII, TBP, GuSCN, MIL-125	LED	27.60	This work

Table 4. Photovoltaic performances of the DSSCs at 6000 lx with N719 dye, pt CE, and a I^-/I_3^- redox couple.

recombination in QSE of DSSCs. This increased recombination rate also accounts for the lower Voc observed in QSE-based DSSCs compared to those with LE, as a higher recombination rate typically results in reduced V_{OC}[50].

[a] The cells were illuminated at a light intensity of 100 mW/cm² and utilized Pt as the CE. [b] BDC = 1,4-benzenedicarboxylic acid or terephthalic acid; [c] bnbip = 2,6-bis(1-(naphthalen-2-ylmethyl)−1*H*-benzo[d]imidazol-2-yl)pyridine; [d] mpi = 5-methoxy-1-(pyridin-4-yl)−1*H*-indole; [e] BTC = 1,3,5-benzenetricarboxylic acid or trimesic acid; [f] no dye concentration and/or soaking time was indicated in the paper.

In addition, the DSSCs were tested under low-light conditions - at 1000, 3000 and 6000 lx - with a dimmable LED light source. The photovoltaic parameters for these conditions are listed in Table 3, which also includes average values and the highest PCE achieved. It is noteworthy that the DSSCs with MIL-125 (QSE) performed better than those with the standard LE. At 6000 lx, the average PCE for QSE was 25.9%, with a peak value of 27.6%, while the LE-based DSSCs achieved an average PCE of 16.94% with the highest at 21.29%. This level of PCE at 6000 lx under LED light is unprecedented for a DSSCs with N719 dye, Pt CE and I^-/I_3^- electrolyte. For comparison, see Table 4 for the performance results of other researchers under similar low-light conditions.

To evaluate the stability of MIL-125 based QSE as an electrolyte, the photovoltaic parameters of DSSCs were periodically measured over a 60-day period (1440 h). The results are shown in Fig. 6. Both QSE and LE-based DSSCs exhibited a slight increase in Voc after 60 days (Fig. 6a). QSE demonstrated a very stable fill factor (FF), while the FF of LE decreased significantly from 71.7 to 66.1% (Fig. 6b). The short-circuit current density of LE dropped substantially from 18.01 to 7.21 mA/cm², whereas based QSE experienced a more moderate decline in J_{SC} from 20.97 to 15.51 mA/cm² (Fig. 6c). Overall, the PCE of based QSE decreased by 21.1% (from 10.51 to 8.29%), while LE showed a much larger decrease of 58.9% (from 9.14 to 3.76%). This indicates a notable improvement in photovoltaic stability for DSSCs using MIL-125 as QSE (Fig. 6d).

Additionally, when tested under dimmed light conditions of 6000 lx, QSE of DSSCs were found to be exceptionally more stable than LE-based devices, retaining over 73% of their initial PCE after 1200 h (Fig. 7). In contrast, LE devices maintained only 53% of their initial PCE after the same period. It is suggested that MIL-125 particles effectively slow down electrolyte evaporation and leakage, thereby supporting the long-term performance of DSSCs.

We also examined the physical and chemical characteristics of MIL-125 after over 4380 h of use, employing XRD, FTIR, SEM, and XPS analysis, as shown in Figures S2 to S5. To carry out this assessment, we dismantled the DSSCs and retrieved the QSE, which serves as a crucial component in the performance of DSSCs by providing ionic conductivity while maintaining a more stable structure compared to liquid electrolytes. The sample was washed with ethanol and then centrifuged at 7000 rpm for 5 min, a process repeated three times to ensure thorough cleaning of any impurities or residual materials. The recovered MIL-125 particles were then dried in a vacuum oven at 70 °C overnight to remove any remaining solvent.

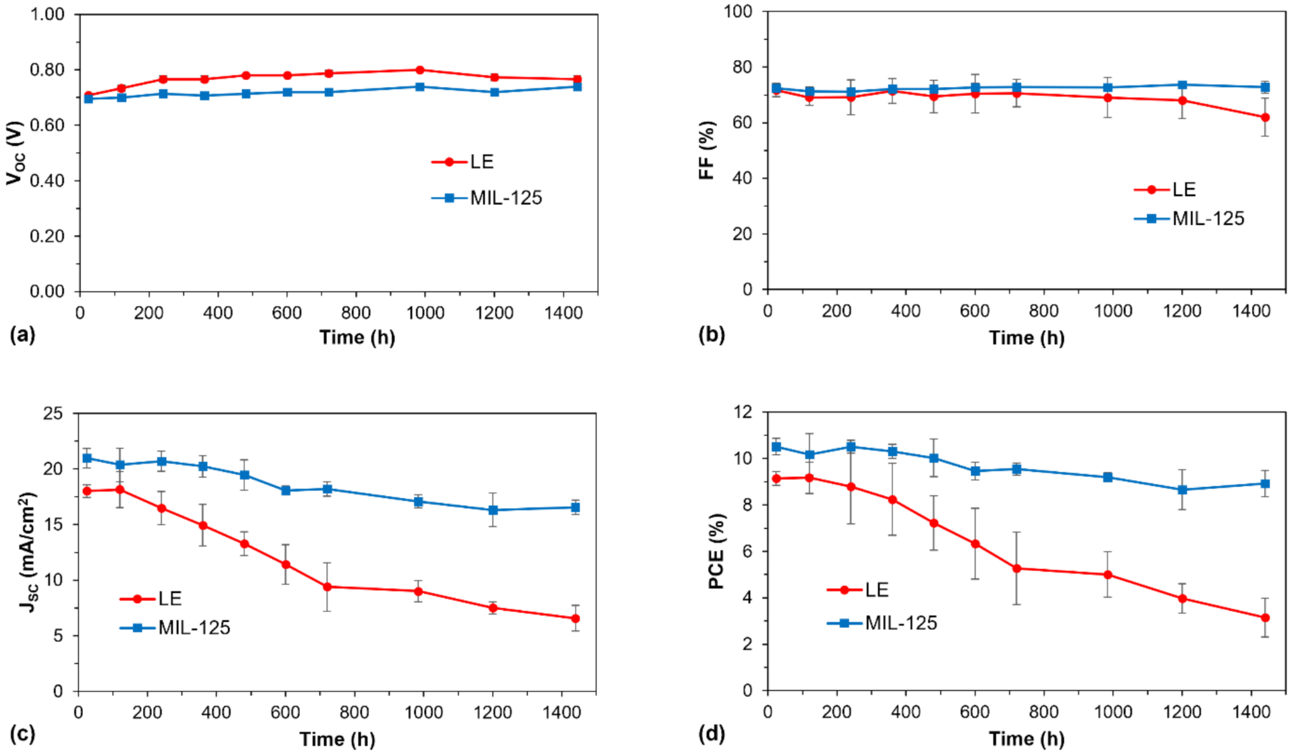

Fig. 6. The stability of the photovoltaic performance of MIL-125 based QSE and LE based DSSCs under AM1.5 100 mW/cm^2 conditions: (**a**) V_{OC} vs. time, (**b**) J_{SC} vs. time, (**c**) FF vs. time, and (**d**) PCE vs. time.

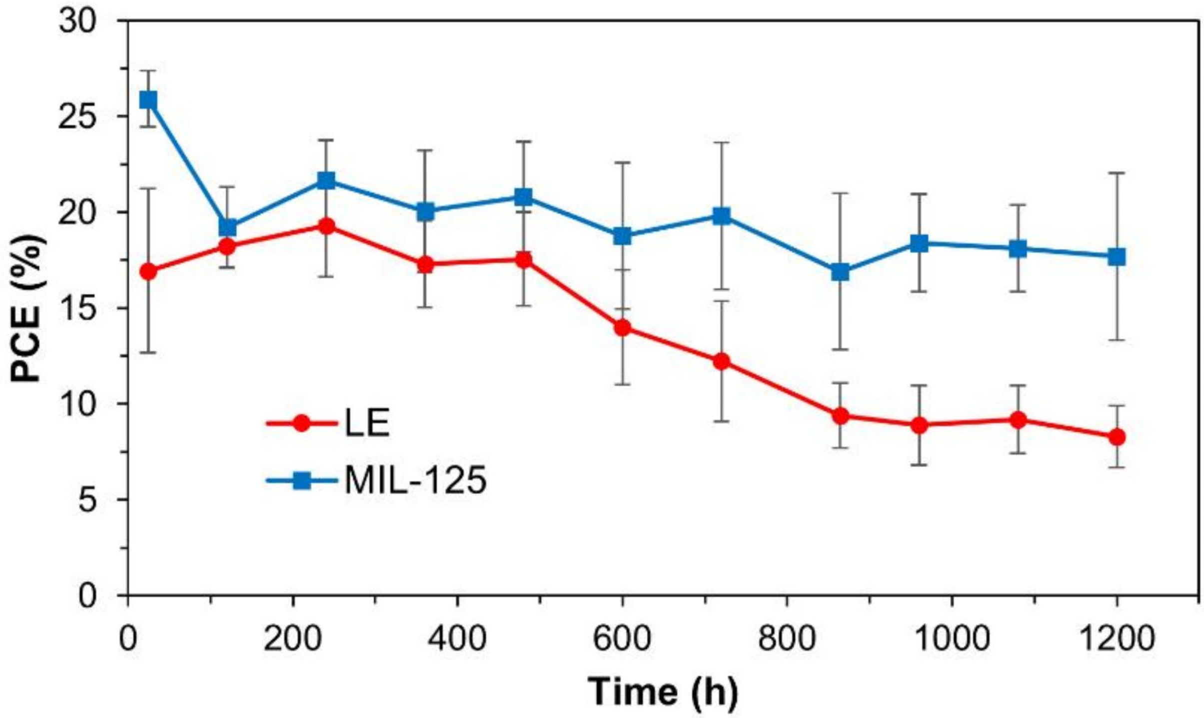

Fig. 7. The stability of the photovoltaic performance of based QSE and LE based DSSCs at 6000 lx.

The powder XRD pattern, shown in Figure S2, closely matches that of the synthesized MIL-125, with no additional peaks, indicating that the MIL-125 structure remained intact after the long-term stability tests. The absence of new peaks suggests that the material did not degrade or undergo any significant changes in crystallinity over the extended testing period. This result is further supported by the FTIR analysis (Figure S3), which shows that the characteristic functional groups of MIL-125 were preserved, indicating no chemical degradation. Additionally, the XPS analysis (Figure S4) confirmed the stability of the surface composition, with no significant shifts in the binding energies, which further indicates the retention of the material's integrity. The SEM images (Figure S5) also demonstrated that the morphology of the MIL-125 particles remained unchanged, with no signs of aggregation or physical damage.

Together, these findings confirm that MIL-125 maintains its structural, chemical, and morphological stability even after extended exposure to the conditions within the DSSCs, reinforcing its potential for use in long-term applications. The stability of MIL-125, particularly in the QSE environment, is crucial as it ensures the continued efficiency and performance of DSSCs over time, making it an excellent candidate for future energy storage and conversion technologies.

Conclusions

In conclusion, a QSE was successfully developed for the first time by simply mixing a metal-organic framework, MIL-125, with an I^-/I_3^- LE at room temperature. This innovation addresses critical stability and leakage issues in DSSCs. The combination of MIL-125 and the electrolyte enhances ionic conductivity, which facilitates more efficient charge transfer and improves the incident photon-to-current conversion efficiency by strengthening the interface interaction between the dye-loaded photoanode and the QSE. Experimental results show that the MIL-125@Electrolyte configuration leads to reduced charge-transfer resistance in the assembled DSSCs. Photovoltaic testing revealed a significant increase in PCE, achieving up to 10.51% (with a maximum of 10.99%) using the N719 dye, thanks to a boosted short-circuit current density of 20.97 mA/cm² and improved long-term stability. Furthermore, when tested under dimmed 6000 lx LED light conditions, the MIL-125-based QSE DSSCs demonstrated an unprecedented PCE of 27.6% with the N719 sensitizer.

Data availability

The datasets used and/or analyzed during the current study available from the corresponding author on reasonable request.

Received: 16 October 2024; Accepted: 10 February 2025

References

1. Ren, Y. et al. Hydroxamic acid pre-adsorption raises the efficiency of cosensitized solar cells. *Nature* **613**, 60–65. https://doi.org/10.1038/s41586-022-05460-z (2023).
2. Michaels, H. et al. Dye-sensitized solar cells under ambient light powering machine learning: towards autonomous smart sensors for the internet of things. *Chem. Sci.* **11**, 2895–2906. https://doi.org/10.1039/C9SC06145B (2020).
3. Ebenezer Anitha, A. & Dotter, M. A review on liquid electrolyte stability issues for commercialization of dye-sensitized solar cells (DSSC). *Energies* **16**, 5129. https://doi.org/10.3390/en16135129 (2023).
4. Wu, J. et al. Progress on the electrolytes for dye-sensitized solar cells. *Pure Appl. Chem.* **80**, 2241–2258. https://doi.org/10.1351/pac200880112241 (2008).
5. Lin, F. S. et al. A novel multifunctional polymer ionic liquid as an additive in iodide electrolyte combined with silver mirror coating counter electrodes for quasi-solid-state dye-sensitized solar cells. *J. Mater. Chem. A*. **9**, 4907–4921. https://doi.org/10.1039/D0TA10826J (2021).
6. Venkatesan, S. et al. Quasi-solid-state composite electrolytes with Al_2O_3 and ZnO nanofillers for dye-sensitized solar cells. *Electrochim. Acta*. **380**, 137588. https://doi.org/10.1016/j.electacta.2020.137588 (2021).
7. Wen, J. et al. Ti_3C_2 MXene-reduced graphene oxide composite polymer-based printable electrolyte for quasi-solid-state dye-sensitized solar cells. *ACS Appl. Energy Mater.* **5**, 3329–3338. https://doi.org/10.1021/acsaem.1c03928 (2022).
8. Masud, Kim, K. M. & Kim, H. K. Polymer gel electrolytes based on peg-functionalized ABA triblock copolymers for quasi-solid-state dye-sensitized solar cells: molecular engineering and key factors. *ACS Appl. Mater. Interfaces*. **12**, 42067–42080. https://doi.org/10.1021/acsami.0c09519 (2020).
9. Jiao, S. et al. Development of rapid curing SiO_2 aerogel composite-based quasi-solid-state dye-sensitized solar cells through screen-printing technology. *ACS Appl. Mater. Interfaces*. **12**, 48794–48803. https://doi.org/10.1021/acsami.0c14551 (2020).
10. Raptopoulou, C. P., Metal-Organic & Frameworks Synthetic methods and potential applications. *Materials* **14**, 310. https://doi.org/10.3390/ma14020310 (2021).
11. Perera, I. R., Hettiarachchi, C. V. & Ranatunga, R. J. K. U. in *Advances in Solar Energy Research* (eds Himanshu Tyagi, Avinash Kumar Agarwal, Prodyut R. Chakraborty, & Satvasheel Powar) 175–219Springer Singapore, (2019).
12. Du, X. et al. Cooperative Crystallization of Chiral Heterometallic Indium(III)–Potassium(I) metal–Organic frameworks as Photosensitizers in Luminescence sensors and Dye-Sensitized Solar cells. *Cryst. Growth Des.* **16**, 1737–1745. https://doi.org/10.1021/acs.cgd.5b01825 (2016).
13. Spoerke, E. D. et al. MOF-Sensitized solar cells enabled by a Pillared Porphyrin Framework. *J. Phys. Chem. C*. **121**, 4816–4824. https://doi.org/10.1021/acs.jpcc.6b11251 (2017).
14. Abdelhamid, H. N. et al. Towards implementing hierarchical porous zeolitic imidazolate frameworks in dye-sensitized solar cells. *Royal Soc. Open. Sci.* **6**, 190723. https://doi.org/10.1098/rsos.190723 (2019).
15. He, Y., Zhang, Z., Wang, W. & Fu, L. Metal organic frameworks derived high-performance photoanodes for DSSCs. *J. Alloys Compd.* **825**, 154089. https://doi.org/10.1016/j.jallcom.2020.154089 (2020).
16. Nizamudeen, C., Krishnapriya, R., Mozumder, M. S., Mourad, A. H. I. & Ramachandran, T. Photovoltaic performance of MOF-derived transition metal doped titania-based photoanodes for DSSCs. *Sci. Rep.* **13**, 6345. https://doi.org/10.1038/s41598-023-33565-6 (2023).
17. Moloto, W., Mbule, P., Nxumalo, E. & Ntsendwana, B. Enhanced optical and electrochemical properties of FeBTC MOF modified TiO2 photoanode for DSSCs application. *Sci. Rep.* **14**, 11292. https://doi.org/10.1038/s41598-024-61701-3 (2024).

18. Uğur, A., Imer, A. G., Kaya, E., Karataş, Y. & Gülcan, M. Improved efficiency in dye sensitized solar cell (DSSC) by nano-MIL-101(cr) impregnated photoanode. *Z. Naturforsch A*. **77**, 93–104. https://doi.org/10.1515/zna-2021-0175 (2022).
19. Younas, M., Gondal, M. A., Dastageer, M. A. & Helal, A. Metal-organic framework coordinated with cobalt ion as charge recombination retarder in dye-sensitized solar cells. *Int. J. Energy Res.* **46**, 9345–9357. https://doi.org/10.1002/er.7809 (2022).
20. Ho Kim, J. et al. High efficiency and stable solid-state fiber dye-sensitized solar cells obtained using TiO2 photoanodes enhanced with metal organic frameworks. *J. Energy Chem.* **67**, 458–466. https://doi.org/10.1016/j.jechem.2021.10.034 (2022).
21. Ram Kumar, P., Ramasubbu, V., Sahaya Shajan, X. & Mothi, E. M. Porphyrin-sensitized quasi-solid solar cells with MOF composited titania aerogel photoanodes. *Mater. Today Energy*. **18**, 100511. https://doi.org/10.1016/j.mtener.2020.100511 (2020).
22. Wu, J. et al. Metal–organic framework-derived cobalt diselenide as an efficient electrocatalyst for dye-sensitized solar cells. *J. Mater. Sci. : Mater. Electron.* **31**, 12309–12316. https://doi.org/10.1007/s10854-020-03776-y (2020).
23. Hsu, S. H. et al. Platinum-free counter Electrode comprised of Metal-Organic-Framework (MOF)-Derived cobalt sulfide nanoparticles for efficient dye-sensitized solar cells (DSSCs). *Sci. Rep.* **4**, 6983. https://doi.org/10.1038/srep06983 (2014).
24. Ou, J., Xiang, J., Liu, J. & Sun, L. Surface-supported metal–Organic Framework Thin-Film-Derived Transparent CoS1.097@N-Doped Carbon Film as an efficient counter electrode for Bifacial Dye-Sensitized Solar cells. *ACS Appl. Mater. Interfaces*. **11**, 14862–14870. https://doi.org/10.1021/acsami.8b21626 (2019).
25. Bella, F., Bongiovanni, R., Kumar, R. S., Kulandainathan, M. A. & Stephan, A. M. Light cured networks containing metal organic frameworks as efficient and durable polymer electrolytes for dye-sensitized solar cells. *J. Mater. Chem. A*. **1**, 9033. https://doi.org/10.1039/C3TA12135F (2013).
26. Sarwar, S. et al. Transformation of a liquid electrolyte to a gel inside dye sensitized solar cells for better stability and performance. *Thin Solid Films*. **704**, 138024. https://doi.org/10.1016/j.tsf.2020.138024 (2020).
27. Saini, I. & Singh, V. in *Metal-organic framework-based nanomaterials for energy conversion and storage* (eds Ram K. Gupta, Tuan Anh Nguyen, & Ghulam Yasin) 535–562 (Elsevier, 2022).
28. Fan, J. et al. A novel metal–organic gel based electrolyte for efficient quasi-solid-state dye-sensitized solar cells. *J. Mater. Chem. A*. **2**, 15406–15413. https://doi.org/10.1039/C4TA03120B (2014).
29. Dong, Y. J. et al. In situ gelation of Al(III)-4-tert-butylpyridine based metal-organic gel electrolyte for efficient quasi-solid-state dye-sensitized solar cells. *J. Power Sources*. **343**, 148–155. https://doi.org/10.1016/j.jpowsour.2017.01.051 (2017).
30. Li, Z., Che, G., Jiang, W., Liu, L. & Wang, H. Visible-light-driven CQDs@MIL-125(Ti) nanocomposite photocatalyst with enhanced photocatalytic activity for the degradation of tetracycline. *RSC Adv.* **9**, 33238–33245. https://doi.org/10.1039/C9RA05600A (2019).
31. Fu, Y. et al. An amine-functionalized titanium metal–organic framework photocatalyst with visible-light-induced activity for CO_2 reduction. *Angew Chem. Int. Ed.* **51**, 3364–3367. https://doi.org/10.1002/anie.201108357 (2012).
32. Zhao, Y., Cai, W., Chen, J., Miao, Y. & Bu, Y. A. Highly efficient Composite Catalyst constructed from NH2-MIL-125(Ti) and reduced Graphene Oxide for CO2 photoreduction. *Front. Chem.* **7**, 789. https://doi.org/10.3389/fchem.2019.00789 (2019).
33. Song, X., He, J., Wang, Y., Wang, J. & Zhang, S. A novel MIL-125(Ti)-based nanocomposite for enhanced adsorption and catalytic degradation of tetracycline hydrochloride: synergetic mechanism of calcination and the nitrogen-containing reticulated surface layer. *J. Colloid Interface Sci.* **645**, 918–932. https://doi.org/10.1016/j.jcis.2023.05.028 (2023).
34. Yang, Z. et al. Preparation of $BiVO_{4/}$MIL-125(Ti) composite with enhanced visible-light photocatalytic activity for dye degradation. *Appl. Organomet. Chem.* **32**, e4285. https://doi.org/10.1002/aoc.4285 (2018).
35. Huang, J., Huang, D., Zeng, F., Ma, L. & Wang, Z. Photocatalytic MOF fibrous membranes for cyclic adsorption and degradation of dyes. *J. Mater. Sci.* **56**, 3127–3139. https://doi.org/10.1007/s10853-020-05473-x (2021).
36. Dan-Hardi, M. et al. A New Photoactive Crystalline highly porous Titanium(IV) Dicarboxylate. *J. Am. Chem. Soc.* **131**, 10857–10859. https://doi.org/10.1021/ja903726m (2009).
37. Rodríguez, N. A., Parra, R. & Grela, M. A. Triethylamine as a tuning agent of the MIL-125 particle morphology and its effect on the photocatalytic activity. *SN Appl. Sci.* **2**, 1881. https://doi.org/10.1007/s42452-020-03683-1 (2020).
38. Al-Taweel, S. S., Saud, H. R., Kadhum, A. A. H. & Takriff, M. S. The influence of titanium dioxide nanofiller ratio on morphology and surface properties of TiO2/chitosan nanocomposite. *Results Phys.* **13**, 102296. https://doi.org/10.1016/j.rinp.2019.102296 (2019).
39. Sun, Y. et al. Synergistic effect of oxygen vacancy and high porosity of nano MIL-125(Ti) for enhanced photocatalytic nitrogen fixation. *Angew Chem. Int. Ed.* **63**, e202316973. https://doi.org/10.1002/anie.202316973 (2024).
40. Fu, Z., Li, Y., Huang, L., Zhang, W. & Weng, L. Three-Dimensional Porous Structural Polyvinylidene Fluoride-Blending Ethylene Carbonate and MIL-125 (Ti) Composite membrane-based gel polymer Electrolyte for Lithium Metal Battery. *J. Electrochem. Soc.* **170**, 120504. https://doi.org/10.1149/1945-7111/ad0ff3 (2023).
41. Liao, X. et al. A Ti-based bi-MOF for the tandem reaction of H2O2 generation and catalytic oxidative desulfurization. *Catal. Sci. Technol.* **10**, 1015–1022. https://doi.org/10.1039/C9CY02318F (2020).
42. Sonigara, K. K. et al. Anisotropic one-Dimensional Aqueous Polymer Gel Electrolyte for Photoelectrochemical devices: improvement in hydrophobic TiO2–Dye/Electrolyte interface. *ACS Appl. Energy Mater.* **1**, 3665–3673. https://doi.org/10.1021/acsaem.8b00444 (2018).
43. Soderberg, J. N., Co, A. C., Sirk, A. H. C. & Birss, V. I. Impact of Porous Electrode properties on the Electrochemical transfer coefficient. *J. Phys. Chem. B*. **110**, 10401–10410. https://doi.org/10.1021/jp060372f (2006).
44. Huo, Z. et al. Low molecular mass organogelator based gel electrolyte gelated by a quaternary ammonium halide salt for quasi-solid-state dye-sensitized solar cells. *J. Power Sources*. **195**, 4384–4390. https://doi.org/10.1016/j.jpowsour.2009.12.107 (2010).
45. Petrii, O. A., Nazmutdinov, R. R., Bronshtein, M. D. & Tsirlina, G. A. Life of the Tafel equation: current understanding and prospects for the second century. *Electrochim. Acta*. **52**, 3493–3504. https://doi.org/10.1016/j.electacta.2006.10.014 (2007).
46. Liberatore, M. et al. Using EIS for diagnosis of dye-sensitized solar cells performance. *J. Appl. Electrochem.* **39**, 2291–2295. https://doi.org/10.1007/s10800-009-9806-5 (2009).
47. Arof, A. K. et al. Quasi solid state dye-sensitized solar cells based on polyvinyl alcohol (PVA) electrolytes containing I^- /I_3^- redox couple. *Opt. Quant. Electron.* **46**, 143–154. https://doi.org/10.1007/s11082-013-9723-z (2014).
48. Osman, Z., Ibrahim, Z. A. & Arof, A. K. Conductivity enhancement due to ion dissociation in plasticized chitosan based Polymer electrolytes. *Carbohydr. Polym.* **44**, 167–173. https://doi.org/10.1016/S0144-8617(00)00236-8 (2001).
49. Bisquert, J. Interpretation of the recombination lifetime in halide perovskite devices by correlated techniques. *J. Phys. Chem. Lett.* **13**, 7320–7335. https://doi.org/10.1021/acs.jpclett.2c01776 (2022).
50. Baptayev, B., Adilov, S. & Balanay, M. P. Surface modification of TiO_2 photoanodes with In^{3+} using a simple soaking technique for enhancing the efficiency of dye-sensitized solar cells. *J. Photochem. Photobiol A*. **394**, 112468. https://doi.org/10.1016/j.jphotochem.2020.112468 (2020).
51. Selvaraj, B. et al. Effect of an aqueous copper gel electrolyte with cobalt metal organic framework based additive on performance of aqueous-dye-sensitized solar cells. *Sol Energy*. **236**, 586–598. https://doi.org/10.1016/j.solener.2022.03.034 (2022).
52. Kesavan, M., Sannasi, V., Kathiresan, M. & Ramesh, M. Metal-organic framework (Mn-BTC MOF) incorporated polymer gel electrolytes for dye-sensitized solar cells: preparation and device performances. *Bull. Mater. Sci.* **46**, 90. https://doi.org/10.1007/s12034-023-02924-4 (2023).
53. Nguyen, T. D., Lan, Y. P. & Wu, C. G. The function of chalcogenophene in the cyclomatelated ring of the cycloruthenated dyes applied in dye-sensitized solar cell. *Inorg. Chem.* **60**, 11328–11337. https://doi.org/10.1021/acs.inorgchem.1c01293 (2021).
54. Desta, M. B. et al. Pyrazine-incorporating panchromatic sensitizers for dye sensitized solar cells under one sun and dim light. *J. Mater. Chem. A*. **6**, 13778–13789. https://doi.org/10.1039/c8ta04774j (2018).

55. Tingare, Y. S. et al. New acetylene-bridged 9,10-conjugated anthracene sensitizers: application in outdoor and indoor dye-sensitized solar cells. *Adv. Energy Mater.* **7**, 1700032. https://doi.org/10.1002/aenm.201700032 (2017).
56. Chandra Sil, M. et al. Enhancement of power conversion efficiency of dye-sensitized solar cells for indoor applications by using a highly responsive organic dye and tailoring the thickness of photoactive layer. *J. Power Sources*. **479**, 229095. https://doi.org/10.1016/j.jpowsour.2020.229095 (2020).
57. Wubie, G. Z. et al. Metal-free organic dyes with double auxiliary acceptors for high-performance dye-sensitized solar cells. *Solar RRL*. **8**, 2300913. https://doi.org/10.1002/solr.202300913 (2024).
58. Wubie, G. Z. et al. Structural engineering of organic D-A-pi-A dyes incorporated with a dibutyl-fluorene moiety for high-performance dye-sensitized solar cells. *ACS Appl. Mater. Interfaces*. **13**, 23513–23522. https://doi.org/10.1021/acsami.1c00559 (2021).

Acknowledgements

This research was funded by the Science Committee of the Ministry of Science and Higher Education of the Republic of Kazakhstan (Grant Nos. AP23490505 (B.B.) and BR24993138 (M.P.B.) and Nazarbayev University under the Faculty Development Competitive Research Grant Program (Grant No. 20122022FD4122 (M.P.B)).

Author contributions

A.I., Z.I., U.A., Y.T. - Conceptualization, methodology, software, validation, formal analysis, investigation, resources, data curation, visualization, writing—original draft preparation; Y.T., B.B., and M.P.B. - supervision; B.B and M.P.B. - writing—review and editing, visualization, project administration, funding acquisition.

Declarations

Competing interests

The authors declare no competing interests.

Additional information

Supplementary Information The online version contains supplementary material available at https://doi.org/10.1038/s41598-025-89913-1.

Correspondence and requests for materials should be addressed to B.B. or M.P.B.

Reprints and permissions information is available at www.nature.com/reprints.